Submitted to Advanced Materials

Revealing the defect-driven ferroelectric mechanisms of Aluminum Nitride

Bogdan Dryzhakov,[1*] Chloe Skidmore,[2] Drew Behrendt,[3] Sebastian V. Calderon,[4] Leonard C. Jacques,[6] Erdem Ozdemir,[2] John Hayden,[2] Ian Mercer,[2] Ali Mohammadi Dinani,[5] Ilia Ivanov,[1] John Lasseter,[1] Bernadeta Srijanto,[1] Alireza Sepehrinezhad,[6] GaUn Jeong,[5] Betul Akkopru Akgun,[2] Andrew M. Rappe,[3] Adri C.T. van Duin,[5,6] Susan Trolier-McKinstry,[2] Elizabeth C. Dickey,[4] Steven Randolph,[1] Jon-Paul Maria,[2] Kyle P. Kelley[1*]

[1] Center for Nanophase Materials Sciences, Oak Ridge National Laboratory, Oak Ridge, Tennessee 37831, USA.
[2] Department of Material Science and Engineering, The Pennsylvania State University, University Park, PA 16802, USA.
[3] Department of Chemistry, University of Pennsylvania, Philadelphia, PA 19104, USA.
[4] Carnegie Mellon University, Department of Materials Science and Engineering, Pittsburgh, PA, USA.
[5] Department of Mechanical Engineering, The Pennsylvania State University, University Park, PA 16802, USA.
[6] Department of Engineering Science & Mechanics, The Pennsylvania State University, University Park, PA 16802, USA.

[*] kelleykp@ornl.gov, dryzhakovb@ornl.gov

Keywords: Ferroelectrics, Aluminum nitride, Ion irradiation, Defects, Thin films

Abstract:

Wurtzite III-nitride compounds are CMOS-compatible with widespread industrial interest to exercise ferroelectricity, despite their polar structure being highly resistant to polarization reversal. Here, we induce and tune ferroelectric properties in w-AlN *via* direct-write ion-beam processing, using nanoscale patterned defect engineering as a post-growth alternative to conventional cation substitution. Nanometric piezoresponse spectroscopy of the focused He^+ beam patterned defect concentrations in ferroelectric $Al_{0.92}B_{0.08}N$ measures a localized 10x enhancement in effective piezoresponse and 40% reduction in switching barrier. The irradiation-induced point defects convert piezoelectric AlN into a ferroelectric system with site-saturated nucleation and raise the dielectric susceptibility, switched polarization, and effective piezoelectric coefficient. Enhanced defect-lattice interactions in AlN increase carrier conduction and phonon scattering loss but preserve long-range crystallinity. Based on atomistic analysis of nudged elastic band density functional theory calculations and reactive force field simulations, both nitrogen vacancies and defect complexes disrupt bond ordering, facilitating a line-by-line low-barrier switching of pristine AlN.

Main Text:

Wurtzite ferroelectrics such as aluminum nitride (AlN) exhibit exceptional spontaneous polarization (>120 μC cm^{-2}) at nanoscale thicknesses, a wide bandgap (~6 eV), and thermal stability up to ~1000°C.[1,2] Moreover, complementary metal-oxide semiconductor (CMOS)-compatible AlN thin films can be prepared via back-end-of-line compatible processes, such as low temperature RF-sputtering[3], for a variety of applications including electronic systems for high-power transistors[4,5] and sensors[6]; photonic systems for ultraviolet optoelectronics[7], waveguides[8], and modulators[9]; and acoustic wave resonator systems[10]. The strong ionic-covalent bonding of AlN makes it resistant to polarity inversion, which is beneficial for applications in harsh environments and for tamper resistant memory.[11] In turn, achieving polarization reversal in AlN incurs a significant energetic cost. This high ferroelectric coercivity is further complicated by its proximity to the dielectric breakdown strength (~8 MV cm^{-1}), such that microelectronic and nonlinear optical devices encounter tolerance and endurance limitations for polarization reversal.[12]

Breakthroughs in structure engineering demonstrated the tunability of the ferroelectric coercive field (E_c) of alloyed AlN down to ~5 MV cm^{-1} and ~2 MV cm^{-1} with boron[2] and scandium[13] alloying, respectively, motivating inquiry into the mechanisms of polarization reversal of the AlN system. The energy barrier for intrinsic switching of polarity is associated with collectively displacing metal ions through the (0001) basal plane.[14] For $Al_{1-x}Sc_xN$, switching is facilitated by the reduction of c/a-axis ratio, effectively bringing the Al ions closer to a domain inversion, and by increased bond ionicity reducing lattice stiffness.[15-17] Recent studies have demonstrated that $Al_{1-x}B_xN$ ferroelectric behavior is governed by local structural distortions, rather than a global structural change and soft mode instability.[18-20] These results are suggestive of the possibility that defects, such as those introduced by irradiation, may lower polarization switching pathways within the rigid wurtzite AlN structure.[21,22]

The localized effects of defects are also evidenced by the nucleation-limited domain growth[20], which also contributes to a ferroelectric wake-up process[18,23]. During "wake-up", charged mobile species can engage in electrochemical processes that influence nucleation. Typically, after ~10^5 cycles, AlN-based ferroelectrics encounter a rise in leakage current[24] and fatigue, accompanied by progressive nitrogen vacancy formation[25], which has been linked in some cases to a filamentary resistive switching mechanism in Sc cation-substituted AlN.[26] Post-growth defect engineering may be a key strategy for tuning ferroelectricity in wurtzite materials.

Accordingly, this study utilizes a focused ionizing beam of helium ions to kinetically displace lattice ions through high-energy collisions within thin films of AlN and $Al_{0.92}B_{0.08}N$. The applicability of this technique to enhance switching in wurtzite ferroelectrics is investigated as a potentially transformative processing method for microelectronics, offering precisely localized nanoscale enhancements of ferroelectric performance. Incident 25 keV-energy helium ions induce kinetic transformations in defect chemistries through ionization, bond breaking, and atom displacement, driving the material into configurations inaccessible to conventional thermodynamic and electrochemical processes. Through combined experimental and computational analysis, this study shows that irradiation-induced point defects reduce the energy barrier for polarization switching in AlN by localized, columnar switching along the polar axis. Despite these local perturbations, the strong lattice restoring forces in AlN inhibit the global lattice softening or the onset of low-frequency 'soft modes' commonly associated with phase transitions in conventional ferroelectrics. As a result, the crystal structure remains robust, enabling defect-driven tunability of ferroelectric properties and enhanced piezoresponse in a nanoscopic direct-write format without compromising polar lattice stability.

Direct-write ferroelectricity in AlN and $Al_{0.92}B_{0.08}N$ *via* helium ion irradiation:

Using focused ion beams to generate point defects in wurtzite AlN thin films tests the defect-based mechanisms of the ferroelectric energy barrier, where local perturbations introduce heterogeneous domain inversion pathways.[18,19] We propose modifying the wurtzite lattice by the interaction of high-energy helium ions (Figure 1A) to create defects as local domain nucleation sites, which activates ferroelectricity in pristine AlN and enhances ferroelectricity of $Al_{0.92}B_{0.08}N$ films. Estimation of the interactions between helium ions and atomic sites within the AlN lattice are as shown in Figures S1 as Stopping and Range of Ions in Matter (SRIM) simulations. Vacancy formation occurs throughout the ion's trajectory into the backing electrode and silicon substrate, minimizing doping of the AlN thin film.

While ferroelectric switching in AlN can be enabled under special conditions, such as elevated temperatures[27] and proximity ferroelectricity[28], the as-grown AlN used here does not display ferroelectricity at room temperature. Upon helium-ion irradiation (Figure 1B), an induced concentration of defects activates AlN's ferroelectric response. With greater irradiation dose, the film exhibits both accelerated switching kinetics and a marked increase in switched polarization, consistent with a larger switched volume and a higher density of active nucleation sites. Kolmogorov–Avrami–Ishibashi analysis of switching dynamics (Figure S2) yields Avrami exponents ($n \approx 1$) at both 500 and 1000 ions nm^{-2}, identifying a nucleation-limited switching regime dominated by percolative nucleation with negligible domain-wall propagation. This mechanism contrasts sharply with scandium- or boron-alloyed AlN ($n \approx 1.7$), which show evidence of both nucleation and significant domain growth. As highlighted in band-excitation piezoresponse spectroscopy (BEPS) (Figure 1C and 1D), defects induced *via* ion irradiation are capable of activating ferroelectricity in AlN and reducing coercive voltage in $Al_{0.92}B_{0.08}N$.

Utilizing a helium ion microscope with a sub-nanometer beam diameter (~0.5 nm), this technique enables precise nanoscale patterning due to minimal lateral dispersion of helium ions within the first 30 nm of the material. The lithographic pattern shown in Figure S3 defines the raster path of the helium ion beam on a pristine 30 nm AlN thin film at a dose of ~1000 ions nm^{-2}, resulting in the modified surface shown in Figure 1E. BEPS spatially maps the ferroelectric behavior across the patterned He-ion irradiated region (Figure 1E), measuring two voltage sweep cycles at each pixel across the image. Domain inversion in the ferroelectric region fabricated through irradiation-based direct writing is evidenced by a reversal in phase after applying -20V, as

shown in the corresponding phase maps before and after voltage application (Figure S3). Accordingly, the coercive field mapping reveals a relatively homogeneous coercive voltage across the irradiated region, while the pristine area remained piezoelectric with no observed polarization reversal.

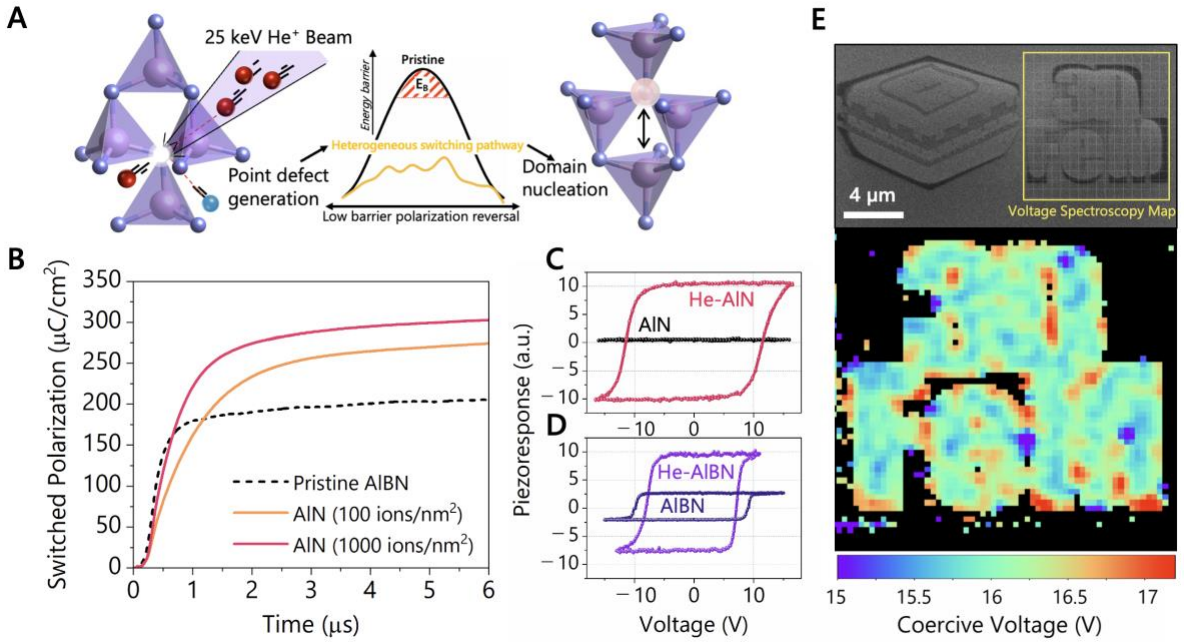

Figure 1: Direct-write ferroelectricity in AlN and enhanced $Al_{0.92}B_{0.08}N$ *via* helium ion irradiation. (A) Schematic illustration of energy barriers in pristine versus defective lattices, highlighting how defects distribute across the lattice as low-energy barrier, localized polarization switching. (B) The measured time-resolved ferroelectric switching in irradiated AlN thin films compared to as-grown $Al_{0.92}B_{0.08}N$, collected after 300 switching cycles. (C) BEPS loops of pristine AlN, confirming the absence of ferroelectric behavior under the switching conditions utilized, and of helium ion-irradiated AlN, demonstrating helium-ion-irradiation-induced ferroelectricity. (D) BEPS loops of pristine and irradiated $Al_{0.92}B_{0.08}N$, showing enhanced ferroelectricity. (E) Top: Helium-ion microscopy image of the helium-ion beam patterned pristine 30 nm AlN thin film at a dose of ~1000 ions nm^{-2}, showcasing the nanoscale patterning capability with minimal lateral dispersion. Bottom: corresponding BEPS mapping of the voltage required to flip the polarization state, demonstrating the coercive field of the irradiated (ferroelectric) region and no switching in the pristine (piezoelectric) region.

Helium ion irradiation enhancement of $Al_{0.92}B_{0.08}N$ ferroelectric capacitors:

The helium ion collisions cumulatively increase defect concentrations as the irradiation dose increases (time-integrated count of helium ions incident per unit area). We test the hypothesis that higher defect concentrations correspond to reduced energy barriers for ferroelectric switching by systematically increasing the irradiation dose. As shown in Figure 2A, lithographically fabricated 1 μm diameter capacitors on a 23 nm $Al_{0.92}B_{0.08}N$ film are subjected to helium ion doses spanning several orders of magnitude up to 10000 ions nm^{-2}. Band-excitation piezoresponse force microscopy is employed to probe the local electromechanical coupling of ion-irradiated regions and conduct voltage spectroscopy.

Electromechanical coupling is measured by applying a variable amplitude AC signal through an AFM probe atop the capacitor. As shown in Figure 2B, ion irradiation induced an apparent ~10x enhancement in electromechanical response. This amplification likely stems in part from defect-mediated domain-wall depinning and activation, but extrinsic contributions (e.g.; mechanical boundary conditions at the back electrode and changes to layer thickness and chemistry) are also expected to play a role. In Figure 2C, the piezoresponse force microscopy (PFM) amplitude-V_{AC} curves are fit to a second-order polynomial, where the linear term coefficient corresponds to the effective piezoelectric coefficient ($d_{33,eff}$) and the quadratic term coefficient (α) captures nonlinearity from processes such as domain-wall motion (bowing/hopping), defect interactions, and dissipative contributions.[29,30] The corresponding fitted coefficients, $d_{33,eff}$ and α, are enhanced with irradiation dose. These trends align quantitatively with the dielectric spectroscopy results in Figure S4: Pristine $Al_{0.92}B_{0.08}N$ has a real permittivity (ε_{init}) of 10.3 ± 0.01 and a small Rayleigh slope (α') of 2.12 x 10^{-4} ± 4.6 x 10^{-6} cm kV^{-1}; a dose of 500 ions nm^{-2} yields ε_{init} = 11.13 ± 0.03 and α' = 2.4 x 10^{-4} ± 1.37 x 10^{-5} cm kV^{-1}, indicating a modest increase in both reversible and irreversible terms; a dose of 1000 ions nm^{-2} maintains ε_{init} = 10.4 ± 0.047, near the pristine baseline value, while returning a 4x increase of irreversible term with α' = 8.65 x 10^{-4} ± 2.09 x 10^{-5} cm kV^{-1}. The pronounced increase in α', together with the reasonable agreement between calculated and measured Rayleigh minor loops (Figure S4), indicates that the dominant contribution is enhanced domain-wall mobility and depinning, although a finite contribution from dielectric loss is also present. Overall, these observations point to an extrinsic, defect-assisted mechanism for irradiation-induced electromechanical enhancement.

Concurrently, the rise in dielectric loss tan(δ) (Figure S4) confers an increased AC conduction (σ_{AC}) and energy dissipation into lattice. Irradiation dose-dependent electrical modulus spectroscopy of $Al_{0.92}B_{0.08}N$ (Figure S5) measures an invariant activation energy of ~1 eV, characteristic of irradiation induced $V_N^{\bullet\bullet\bullet}$ concentrations contributing to σ_{AC}. At low-fields, polarization-electric field (P-E) loops of pristine and irradiated $Al_{0.92}B_{0.08}N$ (Figure S4) are similar, which suggests the enhanced electromechanical response is not solely from increased σ_{AC}. Furthermore, thermally driven contributions are assessed by second harmonic band excitation PFM (Figure S6), which showed negligible contributions from nonlinear processes such as Joule heating.[31,32] Essentially, ion-induced defects produce a greater α' with nucleation site-saturated domain dynamics which, at percolative defect concentrations, enhance the extrinsic susceptibility and boosts $d_{33,eff}$, while increased dielectric loss arises through the nitrogen vacancy-induced conductivity.

Having established that ion irradiation amplifies the sub-coercive electromechanical response, we now examine the systematic reduction in coercive fields *via* defect-mediated nucleation. Coercive field reduction via alloying in $Al_{1-x}B_xN$ thin films plateaus at boron's solubility limit, resulting in a 13% decrease in coercive field from onset of ferroelectricity.[2] In contrast, the defect-mediated switching pathway imposed by helium irradiation in $Al_{0.92}B_{0.08}N$ achieves a 41% reduction in coercive voltage at highest ion dose used, overcoming the intrinsic limitations posed by boron substitution. The coercive field reduction with increasing dose is initially gradual, then steeply reduces at a critical exposure dose (Figures 2D and 2E). At higher doses, ferroelectric wake-up broadens the distribution of switching fields (Figure 2D), indicative of partial switching, and the corresponding PFM phase measurements (Figure S7) confirm that the films initialize from the same polarization state. We anticipate this evolution is governed by defect-structure interactions, prominently the $V_N^{\bullet\bullet\bullet}$ states, as identified by electrical modulus spectroscopy to be the dominant trapping mechanism.

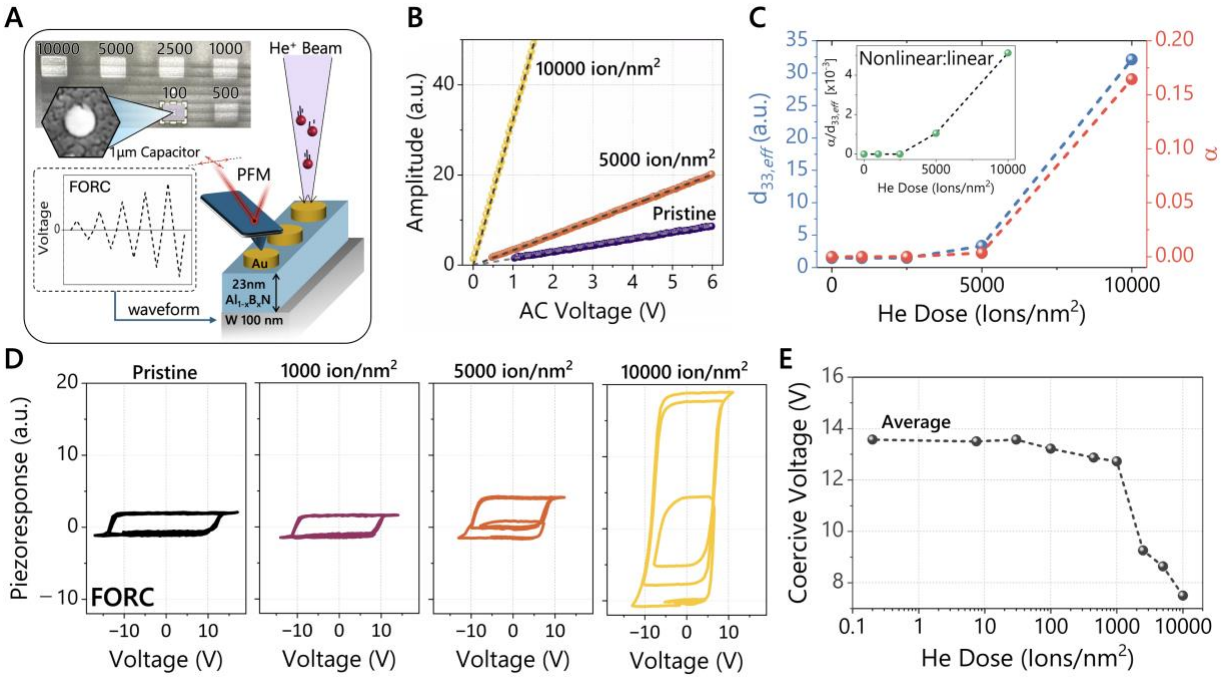

Figure 2: Helium ion irradiation enhancement of $Al_{0.92}B_{0.08}N$ ferroelectric capacitors. (A) Experimental schematic of 1 μm diameter Au capacitors caping 23 nm $Al_{0.92}B_{0.08}N$ thin films with a 100 nm tungsten backing electrode layer. Helium ion microscope image shows the irradiated regions of different ion doses up to 10000 ions nm^{-2}. (B) Amplitude of piezoelectric response versus AC voltage (0.95 Hz) for pristine and high dose irradiated samples. (C) Fitted coefficients of variable AC voltage response curves corresponding to the effective piezoelectric coefficient (d_{33},eff) (left axis) and non-linear coefficient α (right axis). The inset shows the ratio of linear to non-linear piezoelectric response, highlighting the dose-dependent enhancement in nonlinear processes. (D) Piezoelectric hysteresis loops (First-Order Reversal Curves, FORC) for pristine and irradiated samples at ion doses of 1000, 5000, and 10000 ions nm^{-2}. (E) Coercive voltage, reported as the average of the absolute values of the positive and negative coercive voltages, as a function of helium ion dose.

Localized Defect-Structure Evolution Preserves Long-Range Crystalline Order:

The assignment of emissive centers in wide bandgap semiconductors like AlN remains notoriously convoluted, nonetheless, sub-bandgap defect luminescence is generally attributed to point defects such as vacancies and vacancy-impurity complexes. Here, cathodoluminescence (CL) with a focused electron beam to excite sub-bandgap states is used to reveal how radiative defect transitions progressively evolve as a function of helium-ion dose and boron substitution. Tracking defect states that form in AlN and $Al_{1-x}B_xN$ helps build defect-property correlations as it relates to the heterogeneous polarization switching pathways. In Figure 3A, we show low-temperature (10 K) CL spectra of AlN with varying boron concentrations (0%, 8%, 12%, 15%), utilizing 200 nm thick films to provide sufficient bulk emission signal and minimize thin-film optical effects. Boron substituted samples exhibit relatively narrow transition energies at low temperatures, characteristic of localized point defect states. In pristine AlN, charged complexes (V_{Al}-O_N) dominate the CL spectra, whereas boron substitution relatively enhances the emission associated with nitrogen vacancies (~400 nm) as emissions energies common to (V_{Al}-O_N) complexes (~500 nm) are quenched. [33,34] From Figure 3B, we expect that boron substitution and helium ion irradiation may induce defects of fundamentally similar chemistries, most notably nitrogen vacancies, that play a comparable role in enhancing ferroelectricity. The series of CL spectra in Figure 3C show AlN and $Al_{0.92}B_{0.08}N$ with increasing irradiation doses, where irradiated AlN exhibits significant CL quenching and evolving peak intensities that mirror pristine $Al_{0.92}B_{0.08}N$. The similarity in CL profiles between boron-substituted and helium-irradiated AlN (Figure 3B), combined with their parallel dose-dependent behaviors (Figure 3C, S9, and S10), establishes a common defect signature underlying the observed decrease in coercive field and enhancement in measured electromechanical response. This interpretation is further supported by the consistent 1 eV activation energy observed in modulus spectroscopy across increasing helium ion doses (Figure S5), suggesting that irradiation gradually introduces nitrogen vacancies. Nitrogen vacancy spectral signatures thus can serve as a diagnostic tool and engineering guide of ferroelectric properties in AlN.

Having demonstrated that helium-irradiation and boron substitution create similar defect signatures, we now present key structural information using Raman scattering and scanning transmission electron microscopy (STEM) with complementary energy-dispersive X-ray spectroscopy (EDS). Our observations reveal that the tunable functional properties (Figure 1 and

2) are inherent to the localized nature of the induced defect states in the strongly bonded wurtzite structure of AlN, and in consequence, the defects that facilitate ferroelectric domain nucleation are accommodated by the lattice without amorphization. Raman spectroscopy (Figure 3D) of highly-oriented [0001] AlN identifies the E_2 (high) vibrational mode peak [35], [36], and tracks changes induced by boron substitution and helium-irradiation, where diminished peak intensities indicate a loss of phonon coherence and peak shifts indicate long-range structure changes. The E_2 mode centers at ~657 cm^{-1}, though has been reported as high as 666 cm^{-1} with residual epitaxial strain [37] and up to 684 cm^{-1} after Er^{3+} implantation.[38] In our observations, boron alloying in AlN blueshifts the E_2 mode, 20 cm^{-1} at 15% boron; this is correlated with peak broadening and intensity loss attributable to decreased phonon lifetimes.[39] Upon helium irradiation of the AlN and $Al_{0.92}B_{0.08}N$ films, we observe a further broadening and diminishment of the Raman mode intensity without additional peak shifts, suggesting that global strain is negligible.

Several possibilities explain the diminished Raman peak intensity, namely phonon scattering by point defects, non-radiative recombination centers, and increased crystalline disorder such as amorphization or grain fragmentation. However, we observe that the thin films remain crystalline after helium-ion irradiation, as confirmed by High-Angle Annular Dark Field (HAADF)-STEM. Figure 3E and 3F present HAADF-STEM images and diffractograms that confirm the crystalline wurtzite structure after helium-ion irradiation. STEM-based energy-dispersive X-ray spectroscopy (EDS) reveals changes in surface chemistry due to redistribution of surface oxide species, apparent as a layer above the $Al_{0.92}B_{0.08}N$ film, after irradiation. If coercive field were constant, thinning the active $Al_{0.92}B_{0.08}N$ layer from 22 nm to 17 nm would reduce coercive voltage by only ~23%, not the observed 41% by ion-irradiation. In fact, including an oxidized AlN layer, which has lower permittivity and thus a larger electric field drop, would lead to an increased coercive field, contrary to what is observed. Consequently, irradiation-induced vacancies must be structurally localized, while the diminished Raman signal originates from phonon scattering and non-radiative decay of point defects, consistent with the observed CL quenching (Figure 3). These corroborating spectroscopic signatures suggest that structurally localized nitrogen vacancies drive the observed ferroelectric enhancement.

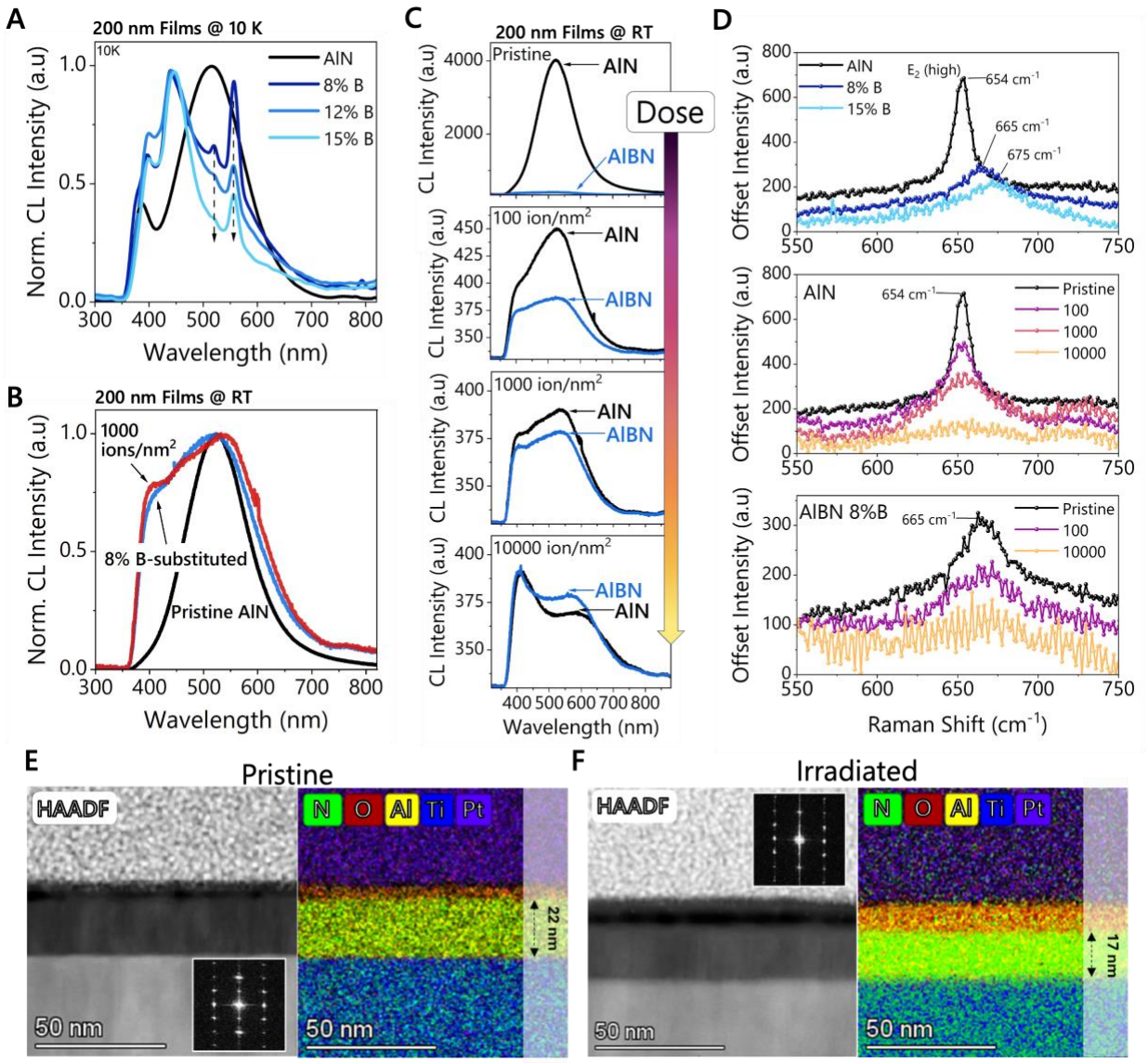

Figure 3: He-ion Induced Defect-Structure Evolution: (A) CL spectra of 200 nm AlN films with varying boron concentrations measured at 10K to discriminate emissive states intrinsic to AlN and boron cation-substitution. (B) Room-temperature (RT) measurements of ferroelectric $Al_{0.92}B_{0.08}N$ and helium-irradiated AlN 200 nm films exhibit similar CL emission profiles, as compared to pristine AlN that is not ferroelectric. (C) Evolution of CL spectra for pristine, 100, 1000, and 10,000 ions nm^{-2} doses for 200 nm thin films of AlN and $Al_{0.92}B_{0.08}N$. True emission intensities are shown at various irradiation doses increasing from top to bottom panels. (D) Structural insights of boron-substitution and helium-irradiation are shown across 3 panels of Raman spectroscopy. The top panel includes Raman scattering at various concentrations of boron substitution: AlN, $Al_{0.92}B_{0.08}N$, and $Al_{0.85}B_{0.15}N$. Helium-ion irradiation effects on Raman scattering are shown in the middle (AlN) and bottom ($Al_{0.92}B_{0.08}N$) panels. HAADF-STEM images and corresponding elemental mapping for $Al_{0.92}B_{0.08}N$ are measured before (E) and after He-irradiation (F).

Theoretical clarification of defect-mediated switching barrier reduction:

The observed reduction in coercive voltage motivates the mechanistic clarification of defect-enabled switching in wurtzite AlN using molecular dynamics simulations and DFT calculations. We propose that defects primarily enable localized domain nucleation, while subsequent domain growth proceeds by column-by-column switching along the polar axis.[18,40]

Using ReaxFF reactive force field molecular dynamics simulations, we irradiated a pristine AlN crystal with eight helium atoms (3.5 keV kinetic energy) to generate a damaged crystal, equilibrated the system, and then applied a sinusoidal electric field to both pristine and damaged crystal to simulate the polarization switching. Simulation snapshots related to the He-irradiation, equilibration, and polarization switching simulations are given in Figure 4A-F. Bombarding the pristine crystal (Figure 4A-C) leads to an equilibrated crystal in Figure 4D that includes a clearly visible line defect. Figures 4E and 4F show that the Al-N-Al connection goes from puckered up to puckered down in response to the change in the direction of the electric field, through which the applied electric field partially reconfigures the damaged crystal. The first two switching barriers are substantially reduced relative to pristine AlN (the average switching barriers for the first two switches are 48% lower for the damaged crystal), in agreement with the experimentally observed reduction in coercive voltage.

Finally, in Figure 4H-J, nudged elastic band (NEB) calculations performed with density functional theory (DFT) provide a mechanistic framework showing how vacancy-type defects generally reduce switching barriers in AlN. In all calculations, barriers decrease with vacancy formation enabling 1D columns of atoms to independently switch along the polar axis, which represents the nucleation and growth mechanisms to effectively induce ferroelectricity in AlN. In the case of simulating complete switching from all up to all down (Figure 4J), both V_N and the (V_{Al}-O_N) complex break the bond ordering enough to allow for line-by-line flipping, breaking the homogeneous switching found for the perfect AlN crystal in the small-scale DFT simulations. While the heterogeneous pathway is favored even in defect-free AlN, defects substantially reduce the energy barriers to access it (up to 43% reduction in barrier for single defects and up to 86% for the coupled V_{Al}-O_N complex). The defect-driven coercive-field reduction trend qualitatively aligns between experiment, ReaxFF, and DFT.

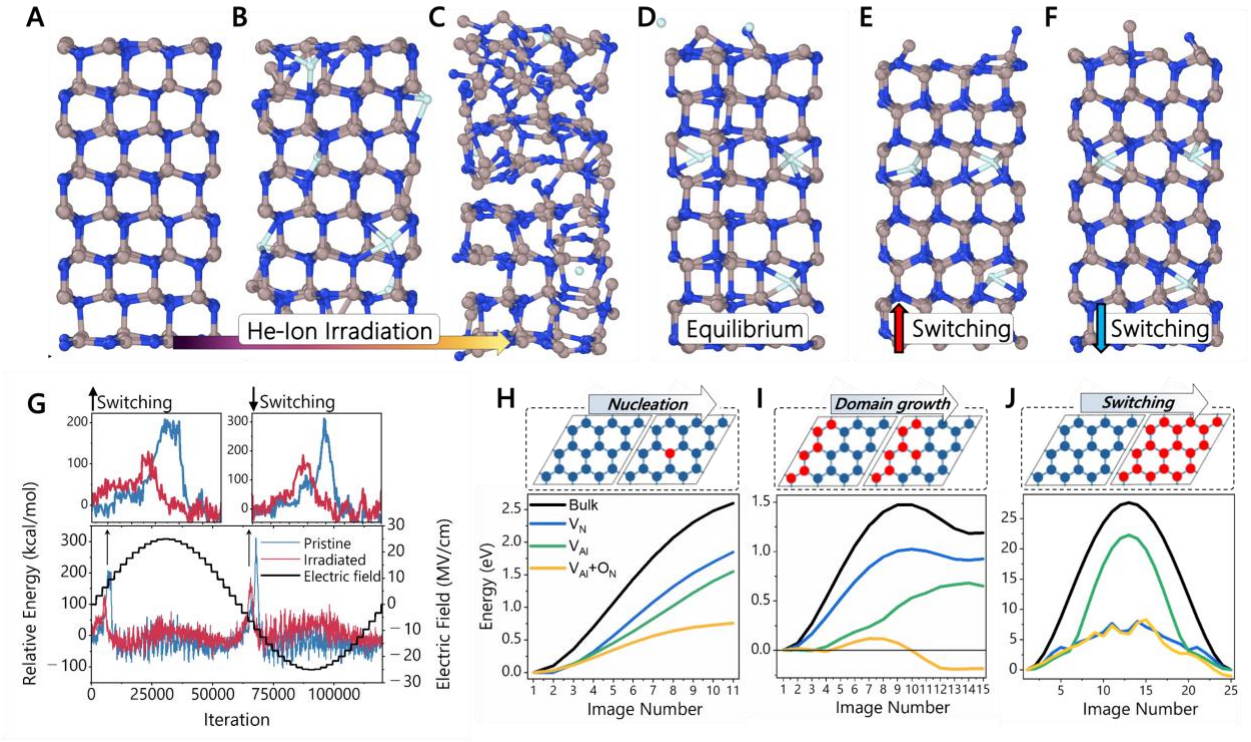

Figure 4: ReaxFF Simulations and DFT-NEB Calculations. (A-F) Simulation snapshots for the irradiation, equilibration, and polarization switching along with the time-series plots of crystals' relative energies in the polarization switching. Simulation snapshots are for the damaged crystal and the time-series plots of relative energies are for the pristine and damaged crystals. Irradiation, equilibration, and polarization switching are done for 500-, 100-, and 1550-frame simulations, respectively where every 100 iterations constitute a frame. Aluminum, nitrogen, and helium atoms are shown in silver, blue, and cyan, respectively. (A) frame 0 of bombardment, showing the pristine crystal; (B) frame 100 of bombardment; (C) frame 500 of bombardment; (D) frame 100 of equilibration, showing the defected crystal returning to a more crystalline structure; (E) frame 300 of the switching under maximum positive electric field (+25 MV cm^{-1}); (F) frame 900 of the switching under maximum negative electric field (−25 MV cm^{-1}). (G) Changes in the switching energy barriers for two successive polarization switches are shown when a sinusoidal electric field is applied. The y-axis for relative energy is on the left, and the y-axis for the applied electric field is on the right. (H-J) DFT-NEB calculations of possible switching pathways with both pure AlN and AlN containing 1 defect site in a 108-atom unit cell. Shown cells are those used in the simulations and are viewed along the polar axis. Blue and red atoms represent entire columns of atoms that are polar up and down, respectively. (H) The energy for a single column of atoms to flip when either containing a defect or not, representing initial domain nucleation. (I) The energy for a single column of atoms to flip along a domain wall, representing domain growth. (J) Energy for switching the entire 108-atom unit cell under a uniformly applied electric field showing the switching pathway is predominantly homogeneous for pristine AlN and V_{Al} but becomes heterogeneous (line-by-line/columnar) for V_N and the V_{Al}–O_N defect complex.

Discussion:

The mechanistic understanding of AlN's ferroelectricity converges experimental results and theoretical models, which support a defect-driven mechanism for polarization reversal. The strongly bonded wurtzite structure of AlN resists lattice softening and flat polar phonon band formation commonly observed in fluorite-based ferroelectrics such as HfO_2 [41,42], so soft-mode dynamics are not the dominant pathway. Instead, helium ion irradiation in AlN introduces point defects that locally disrupt phonon coherence and lower switching barriers while preserving long-range crystalline order. In boron-substituted AlN, ferroelectric dynamics likely arise from a combination of lattice softening and defect-assisted nucleation, with switching barriers further reduced by localized defect states. Here, ion irradiation surpassed the structural limitations of boron alloying, reducing the coercive field of $Al_{0.92}B_{0.08}N$ by 41%. Defects act as heterogeneous nucleation centers and reduce domain-wall pinning barriers, thereby enabling ferroelectric switching and enhancing dynamic polarizability. Higher susceptibility and a larger switched fraction, alongside elevated dissipation and carrier transport, seen as increased phonon losses and leakage currents, constitute a performance trade-off. The spectroscopic signatures identified here provide markers for specific defect populations and local environments; together with the electrical metrics, they establish a framework for defect-based optimization in wurtzite structures. Further, focused ion beams are established as direct-write processes for enhancing ferroelectricity in boron-substituted AlN and inducing ferroelectricity in pristine AlN *via* targeted helium-ion irradiation. Defect-mediated reductions in coercive field thus open a pathway for AlN, and related III-V nitride materials, to serve as multifunctional platforms for advanced electronic and photonic systems requiring active polarization control. In radiation-intensive environments such as space exploration, where defect creation is unavoidable, the relatively large coercive fields and structural radiation hardness typical of wurtzite-structured ferroelectrics offer advantages over other ferroelectric systems. At the same time, radiation resistance does not imply invariance of electrical behavior, and practical deployment must account for the device-level constraints identified here, including increased leakage and potential impacts on electrical fatigue and breakdown.

Methods

Thin film preparation:

$Al_{1-x}B_xN$ and AlN thin films were grown on Si substrates using a custom magnetron sputtering system featuring four 2-inch Kurt J. Lesker MagKeeper cathodes with Al, BN, and W targets. The magnetrons are disposed in a confocal configuration with a 22.5° attack angle with respect to the substrate normal. Al and BN targets are powered by RF-VII RF power supplies, while W back electrodes are powered by an ENI RPG50 pulsed DC supply in DC mode. Si substrates are heated radiantly using a modified AJA XYZ substrate manipulator/heater stage. The process begins with exposing an untreated Si substrate with an RF 1:1 N_2<:Ar plasma at 50 watts for 20 minutes at 350 °C.[2] Next, still at 350°C, a 30 nm seed layer of AlN is grown to establish (0002) texture, followed by 100 nm of W-metal with (110) texture. The W is randomly oriented in-plane with a (110) rocking curve of ~ 1.7°. AlN and $Al_{1-x}B_xN$ films were prepared by co-sputtering from their respective targets at the same temperature.

Piezoresponse Force Microscopy (PFM):

Piezoresponse force microscopy experiments were conducted utilizing Budget Sensor Multi75E-G AFM probes coated with Cr/Pt and a spring constant ~3 N m^{-1}. Band excitation piezoresponse force microscopy was achieved by interfacing the AFM with an arbitrary wave generator and data acquisition system powered by a National Instruments fast DAQ card. Custom software was employed to generate the probing signal and record local response. Band excitation PFM measurements encompassed frequencies spanning from 300 to 400 kHz, followed by application of simple harmonic oscillator fits to the acquired spectra for extracting amplitude and phase information at the resonance frequency. Ambient PFM measurements were conducted utilizing an Oxford Instruments Cypher atomic force microscope and environmentally controlled PFM measurements were conducted using a Bruker Dimension Icon fitted inside a MBRAUN MB200B series glove box.

Helium-ion irradiation:

200 nm samples used in cathodoluminescence and Raman studies: The irradiation was performed using Zeiss Orion NanoFab helium ion microscope (HIM) operating at an acceleration voltage of

25 keV. A beam current of 142 pA was achieved using a spot size setting of 4.29 and the big hole aperture. The dwell time was set to 1 μs per pixel, with a pixel spacing (pitch) of 10 nm.

Thin Film Capacitor Samples (23 nm $Al_{0.92}B_{0.08}N$ and 30 nm AlN): Prior to exposure, a 10 minute oxygen plasma clean was performed to reduce helium ion induced carbon contamination. The irradiation was carried out using the Fibics (Ottawa, Canada) NanoPatterning and Visualization Engine (NPVE). The following common parameters were used for all dosages: 25 keV acceleration voltage, 10 nm pixel spacing, 1 μs dwell time, and 119 pA beam current. Dosage was controlled with repeat raster passes over the irradiated region.

Fabrication of Capacitor Devices:

A combination of electron beam lithography (EBL) and a metal lift off process were used to fabricate the capacitor devices. The substrate was cleaned with acetone and IPA prior to spin-coating it with 950 PMMA A2 electron beam resist (Kayaku, Westborough, MA) at 3000 rpm for 45 s, and baked on a hotplate for 2 minutes at 180°C. Electron beam lithography was performed with a JEOL JBX8100-FS system operating at 100 kV acceleration voltage. A 40 nA beam current and 1000 μC cm^{-2} dose were used to define the geometry of the capacitors. The patterned substrate was developed in 1:3 methyl isobutyl ketone (MIBK): isopropyl alcohol (IPA) for 1 min, rinsed with IPA, and dried with nitrogen, followed by exposure to oxygen plasma for 6 s at 100 W, 10 sccm O_2, and 150 mT. A lift-off process, using acetone and IPA, was carried out following deposition of 5 nm Ti and 20 nm Au by electron beam evaporation.

Cathodoluminescence:

An FEI Quattro environmental SEM with a Delmic Sparc CL collection module, utilizing a parabolic mirror to collect the CL signals from the film upon e-beam excitation, was used. An electron beam with an acceleration voltage of 5 kV (with a beam current of 230 pA) was passed through a hole in the parabolic mirror for sample excitation and an acquisition time of 400 ms per spectrum was used for CL signal collection. The electron beam penetrates approximately 100 nm into the surface of AlN, with subsequent emissions corresponding to various defect states. The spectral coverage is optimized for the visible with a 350 nm cut off from the coating on the Newton BEX2-DD.

Raman Spectroscopy:

Raman spectroscopy was employed as a spectral map consisting of 5 × 5 points collected across the corresponding irradiated area, and the spectra were averaged to obtain representative data. Measurements were performed in backscattering configuration using an upright confocal Raman microscope inVia Qontor (Renishaw, LLC) with a 532 nm excitation laser, 2400 lines mm^{-1} grating, 10 second integration time, and two repetitions to improve the signal-to-noise ratio. The laser was operated at power of 25 mW.

Scanning Transmission Electron Microscopy (STEM):

Cross-sectional samples were prepared using a Ga-focused ion beam, applying an acceleration voltage of 30 kV for trench milling and 2–5 kV for lamella thinning. High-angle annular dark-field scanning transmission electron microscopy (HAADF-STEM) images were acquired using a ThermoFisher Titan-Themis microscope operating at 200 kV. The probe had a convergence angle of 17.9 mrad, and a camera length was selected to achieve acceptance angles between 70–200 mrad. Elemental maps were obtained using energy dispersive X-ray spectroscopy (STEM-EDS) with a Super-X EDS detector. The maps were collected at 512 x 512 pixels resolution, with a dwell time of 10 µs per pixel, over a 10-minute acquisition at 200 keV. Elemental maps were plotted using the integrated intensities of the N, O, Al and Ti - Kα lines and Pt - Lα line.

Density Functional Theory (DFT):

DFT calculations were performed using Quantum Espresso[43] with optimized norm-conserving pseudopotentials from OPIUM.[44,45] The generalized gradient approximation (GGA) of Perdew, Burke, and Ernzerhof (PBE) was used to calculate the exchange correlation energy.[46] Convergence criteria of 1.4×10^{-5} eV $cell^{-1}$ for self-consistent field calculations, and 2.6×10^{-4} eV $Å^{-1}$ and 1.4×10^{-3} eV $cell^{-1}$ for energy and forces, respectively, were used for all calculations. Our simulation cells were 3x3x3 AlN supercells with 108 atoms per cell.

ReaxFF Reactive Force Field Computation:

ReaxFF force field training for AlN: The initial ReaxFF Al-parameters were taken from Hong and co-workers,[47] while the initial N-parameters were taken from the ReaxFF protein description from Monti and co-workers.[48] To train the Al/N interactions, we created a ReaxFF training set containing DFT-based volume/energy equations of state for the wurtzite and the cubic AlN-phase.

Figure S15 compare the DFT and ReaxFF equations of state and relative stabilities of these AlN phases after training, showing that ReaxFF correctly reproduces the DFT data that describe the wurtzite phase as the global minimum, with a phase transition to the cubic phase at decreasing volume. ReaxFF was also trained against the heat of formation of AlN-wurtzite and the neutral N-vacancy energy. For these, ReaxFF predicts values of -62.7 kcal $atom^{-1}$ and +112.8 kcal mol^{-1}, respectively, compared to DFT values of -73.02 kcal $atom^{-1}$ and +120.1 kcal mol^{-1}. The N-vacancy energy uses N_2 as a gas-phase reference. ReaxFF training was performed using the standalone ReaxFF code, which uses a single-parameter search method.[49] In this force field development we used the ACKS2 charge calculation method [50] instead of the EEM charge calculation method [51] commonly used with ReaxFF to avoid over-polarization of the AlN slab during electric field exposure.

DFT Calculations for ReaxxFF training: To construct the ReaxFF training set for the Al/N binary system, periodic density functional theory (DFT) were performed using the Vienna *ab initio* simulation package (VASP).[52] The DFT calculations used the projector augmented wave (PAW) [53] pseudo−potentials and Perdew−Burke−Ernzerhof (PBE) [46] exchange and correlation functional, with an energy cutoff of 520 eV. All calculations were carried out with spin polarization to accurately capture the magnetic structures of the binary systems.

For lattice optimization of ordered bulk crystals, the thermodynamically stable wurtzite (hexagonal) and the metastable rocksalt (cubic) structure were considered. Each structure was subjected to full relaxation of the lattice parameters and atomic positions until the forces on all atoms were below 0.002 eV $Å^{-1}$, and the total energy convergence criterion was set to 2×10^{-4} eV. The optimized bulk geometries and corresponding total energy values were subsequently used to construct a set of equations of states, cohesive energy, and heat of formation dataset. For the equations of state, the lattice parameters of the optimized structures were systematically scaled from 0.90 to 1.10 in increments of 0.01, generating 20 additional configurations for each phase. It captures the mechanical behavior of the system under both compression and expansion, providing comprehensive data for training the ReaxFF force field.

ReaxFF simulation settings: Three types of MD simulations were performed: He-irradiation, equilibration, and polarization switching for which the time-steps were 0.050, 0.250, and 0.250 fs, respectively. A Berendsen thermostat with temperature damping constants of 100 fs, and a simulation temperature of 500 K were used for the equilibration and polarization switching

simulations. For the He-irradiation simulation an NVE ensemble was used with an initial temperature of 300 K.

Electrical Modulus Spectroscopy Measurements:

Modulus spectroscopy was employed to investigate conductivity changes induced by helium ion irradiation in $Al_{0.92}B_{0.08}N$ films using a Solartron Analytical Modulab system. Both pristine and irradiated samples were heated to 280 °C, at which point impedance (Z), electrical modulus (M), admittance, and capacitance (C) were simultaneously measured over a frequency range of 1 mHz to 1 MHz under an applied AC bias of 100 mV. The imaginary component of the electrical modulus, M″, exhibits a characteristic peak at the relaxation frequency, defined as:

$$f_r = \frac{\sigma}{2\pi\varepsilon_0\varepsilon_r}$$

where σ is the conductivity, ϵ_0 is the permittivity of free space, and ϵ_r is the relative permittivity of the film. A shift of this peak toward higher frequencies indicates an increase in the film's conductivity.

Electrical Measurements on Capacitors:

Ferroelectric switching measurements were conducted after electrical modulus spectroscopy measurements. The ferroelectric switching kinetics apparatus consisted of an Agilent 33220A 20 MHz function generator, a 50x Trek Model 2100HF amplifier, and a Tektronix TBS 2000B Series Oscilloscope with 1 ns precision. A custom PUND waveform sequence with a 12.5 μs pulse widthdelay was applied to the function generator. Data curation and fitting experimental data to the simulated models were performed in MATLAB. For Rayleigh analysis, capacitance measurements as a function of AC field were performed using a Hewlett Packard 4284A LCR meter with voltages up to 20 V and a frequency of 10 kHz. Minor P-E loops were acquired with a Radiant Premier II ferroelectric tester with a frequency of 10 kHz and peak field of 1 MV cm^{-1}. Calculated minor loops were obtained using the following equation:

$$P(E) = (\varepsilon'_{init} + \alpha' E_0)E \pm \frac{\alpha'}{2}(E^2 - E_0^2)$$

where P is the dielectric polarization, E is the instantaneous field, E_0 is the amplitude of the driving field, ε'_{init} is the reversible Rayleigh coefficient, and α' is the irreversible Rayleigh coefficient.

Acknowledgments

The defect-induced phenomenon was conceptualized, developed, initially demonstrated, and validated with support by the Center for 3D Ferroelectric Microelectronics (3DFeM), an Energy Frontier Research Center funded by the US Department of Energy, Office of Science, Office of Basic Energy Sciences Energy Frontier Research Centers program under award DE-SC0021118. The piezoresponse force microscopy, scanning electron microscope cathodoluminescence, Raman spectroscopy, and helium ion irradiation research was supported by the Center for Nanophase Materials Sciences (CNMS), which is a US Department of Energy, Office of Science User Facility at Oak Ridge National Laboratory.

Data Availability

The data that support the findings of this study are available from the corresponding author upon reasonable request.

References

1 Islam, M. R. *et al.* On the exceptional temperature stability of ferroelectric $Al_{1-x}Sc_xN$ thin films. *Applied Physics Letters* **118** (2021).

2 Hayden, J. *et al.* Ferroelectricity in boron-substituted aluminum nitride thin films. *Physical Review Materials* **5**, 044412 (2021).

3 Dogheche, E., Rémiens, D., Boudrioua, A. & Loulergue, J. C. Growth and optical characterization of aluminum nitride thin films deposited on silicon by radio-frequency sputtering. *Applied Physics Letters* **74**, 1209-1211 (1999). https://doi.org/10.1063/1.123501

4 Ambacher, O. *et al.* Pyroelectric properties of Al (In) GaN/GaN hetero-and quantum well structures. *Journal of physics: condensed matter* **14**, 3399 (2002).

5 Hickman, A. L. *et al.* Next generation electronics on the ultrawide-bandgap aluminum nitride platform. *Semiconductor Science and Technology* **36**, 044001 (2021).

6 Cimalla, V., Pezoldt, J. & Ambacher, O. Group III nitride and SiC based MEMS and NEMS: materials properties, technology and applications. *Journal of Physics D: Applied Physics* **40**, S19 (2007).

7 Taniyasu, Y., Kasu, M. & Makimoto, T. An aluminium nitride light-emitting diode with a wavelength of 210 nanometres. *nature* **441**, 325-328 (2006).

8 Pernice, W. H. P., Xiong, C., Schuck, C. & Tang, H. Second harmonic generation in phase matched aluminum nitride waveguides and micro-ring resonators. *Applied Physics Letters* **100** (2012).

9 Xiong, C., Pernice, W. H. & Tang, H. X. Low-loss, silicon integrated, aluminum nitride photonic circuits and their use for electro-optic signal processing. *Nano letters* **12**, 3562-3568 (2012).

10 Lin, C.-M. *et al.* Temperature-compensated aluminum nitride Lamb wave resonators. *IEEE transactions on ultrasonics, ferroelectrics, and frequency control* **57**, 524-532 (2010).

11 Parks, D. A. & Tittmann, B. R. Radiation tolerance of piezoelectric bulk single-crystal aluminum nitride. *IEEE transactions on ultrasonics, ferroelectrics, and frequency control* **61**, 1216-1222 (2014).

12 He, F. *et al.* Frequency dependence of wake-up and fatigue characteristics in ferroelectric $Al_{0.93}B_{0.07}N$ thin films. *Acta Materialia* **266**, 119678 (2024). https://doi.org/https://doi.org/10.1016/j.actamat.2024.119678

13 Fichtner, S., Wolff, N., Lofink, F., Kienle, L. & Wagner, B. AlScN: A III-V semiconductor based ferroelectric. *Journal of Applied Physics* **125** (2019).

14 Fichtner, S., Yassine, M., Van de Walle, C. G. & Ambacher, O. Clarification of the spontaneous polarization direction in crystals with wurtzite structure. *Applied Physics Letters* **125** (2024).

15 Jiang, Z., Paillard, C., Vanderbilt, D., Xiang, H. & Bellaiche, L. Designing multifunctionality via assembling dissimilar materials: Epitaxial AlN/ScN superlattices. *Physical review letters* **123**, 096801 (2019).

16 Akiyama, M. *et al.* Enhancement of piezoelectric response in scandium aluminum nitride alloy thin films prepared by dual reactive cosputtering. *Advanced Materials* **21**, 593-596 (2009).

17 Behrendt, D., Banerjee, S., Zhang, J. & Rappe, A. M. Discovery of wurtzite solid solutions with enhanced piezoelectric response using machine learning. *Physical Review Materials* **8**, 055406 (2024).

18 Calderon, S. *et al.* Atomic-scale polarization switching in wurtzite ferroelectrics. *Science* **380**, 1034-1038 (2023). https://doi.org/doi:10.1126/science.adh7670

19 Lee, C.-W., Yazawa, K., Zakutayev, A., Brennecka, G. L. & Gorai, P. Switching it up: New mechanisms revealed in wurtzite-type ferroelectrics. *Science Advances* **10**, eadl0848 (2024).

20 Yazawa, K. *et al.* Anomalously abrupt switching of wurtzite-structured ferroelectrics: simultaneous non-linear nucleation and growth model. *Materials Horizons* **10**, 2936-2944 (2023).

21 Lee, C.-W., Din, N. U., Brennecka, G. L. & Gorai, P. Defects and oxygen impurities in ferroelectric wurtzite Al1− xScxN alloys. *Applied Physics Letters* **125** (2024).

22 Wolff, N. *et al.* Interfacial Polarization Switching in $Al_{0.92}Sc_{0.08}N$/GaN Heterostructures Grown by Sputter Epitaxy. *Advanced Science*, e03827 (2025).

23 Zhu, W. *et al.* Wake-Up in $Al_{1-x}B_xN$ Ferroelectric Films. *Advanced Electronic Materials* **8**, 2100931 (2022). https://doi.org/https://doi.org/10.1002/aelm.202100931

24 Kataoka, J. *et al.* A possible origin of the large leakage current in ferroelectric $Al_{1-x}Sc_xN$ films. *Japanese Journal of Applied Physics* **60**, 030907 (2021).

25 Ren, Q. *et al.* Strain-Controlled Formation Energy and Migration of Nitrogen Vacancy in $Al_{1-x}Sc_xN$: A First-Principles Study. *ACS Applied Materials & Interfaces* **16**, 28838-28844 (2024). https://doi.org/10.1021/acsami.4c03442

26 Guido, R., Mikolajick, T., Schroeder, U. & Lomenzo, P. D. Role of Defects in the Breakdown Phenomenon of $Al_{1-x}Sc_xN$: From Ferroelectric to Filamentary Resistive Switching. *Nano Letters* **23**, 7213-7220 (2023).

27 Zhu, W. *et al.* Strongly temperature dependent ferroelectric switching in AlN, $Al_{1-x}Sc_xN$, and $Al_{1-x}B_xN$ thin films. *Applied Physics Letters* **119** (2021).

28 Skidmore, C. H. *et al.* Proximity ferroelectricity in wurtzite heterostructures. *Nature*, 1-6 (2025).

29 Peters, T., Zhu, W., Checa, M., Collins, L. & Trolier-McKinstry, S. Influence of doping and thickness on domain avalanches in lead zirconate titanate thin films. *Applied Physics Letters* **122** (2023).

30 Li, L. *et al.* Correlation between piezoresponse nonlinearity and hysteresis in ferroelectric crystals at the nanoscale. *Applied Physics Letters* **108** (2016).

31 Kim, Y. *et al.* Nonlinear phenomena in multiferroic nanocapacitors: Joule heating and electromechanical effects. *ACS nano* **5**, 9104-9112 (2011).

32 Chen, Q. N., Ou, Y., Ma, F. & Li, J. Mechanisms of electromechanical coupling in strain based scanning probe microscopy. *Applied Physics Letters* **104** (2014).

33 Koppe, T., Hofsäss, H. & Vetter, U. Overview of band-edge and defect related luminescence in aluminum nitride. *Journal of Luminescence* **178**, 267-281 (2016).

34 Atobe, K., Honda, M., Fukuoka, N., Okada, M. & Nakagawa, M. F-type centers in neutron-irradiated AIN. *Japanese journal of applied physics* **29**, 150 (1990).

35 Filippidis, L. *et al.* Raman frequencies and angular dispersion of polar modes in aluminum nitride and gallium nitride. *Physica status solidi (b)* **198**, 621-627 (1996).

36 Kazan, M., Rufflé, B., Zgheib, C. & Masri, P. Phonon dynamics in AlN lattice contaminated by oxygen. *Diamond and related materials* **15**, 1525-1534 (2006).

37 Yang, S., Miyagawa, R., Miyake, H., Hiramatsu, K. & Harima, H. Raman scattering spectroscopy of residual stresses in epitaxial AlN films. *Applied physics express* **4**, 031001 (2011).

38 Kallel, T., Dammak, M., Wang, J. & Jadwisienczak, W. Raman characterization and stress analysis of AlN: Er^{3+} epilayers grown on sapphire and silicon substrates. *Materials Science and Engineering: B* **187**, 46-52 (2014).

39 Hoque, M. S. B. *et al.* Experimental observation of ballistic to diffusive transition in AlN thin films. *arXiv preprint arXiv:2409.14328* (2024).

40 Behrendt, D., Samanta, A. & Rappe, A. M. Ferroelectric Fractals: Switching Mechanism of Wurtzite AlN. *arXiv preprint arXiv:2410.18816* (2024).

41 Ai, P. *et al.* Point-defect-driven flattened polar phonon bands in fluorite ferroelectrics. *npj Computational Materials* **9**, 119 (2023). https://doi.org/10.1038/s41524-023-01075-8

42 Lee, H.-J. *et al.* Scale-free ferroelectricity induced by flat phonon bands in HfO2. *Science* **369**, 1343-1347 (2020).

43 Giannozzi, P. *et al.* QUANTUM ESPRESSO: a modular and open-source software project for quantum simulations of materials. *Journal of physics: Condensed matter* **21**, 395502 (2009).

44 Rappe, A. M., Rabe, K. M., Kaxiras, E. & Joannopoulos, J. Optimized pseudopotentials. *Physical Review B* **41**, 1227 (1990).

45 Ramer, N. J. & Rappe, A. M. Designed nonlocal pseudopotentials for enhanced transferability. *Physical Review B* **59**, 12471 (1999).

46 Perdew, J. P., Burke, K. & Ernzerhof, M. Generalized gradient approximation made simple. *Physical review letters* **77**, 3865 (1996).

47 Hong, S. & Van Duin, A. C. Atomistic-scale analysis of carbon coating and its effect on the oxidation of aluminum nanoparticles by ReaxFF-molecular dynamics simulations. *The Journal of Physical Chemistry C* **120**, 9464-9474 (2016).

48 Monti, S. *et al.* Exploring the conformational and reactive dynamics of biomolecules in solution using an extended version of the glycine reactive force field. *Physical Chemistry Chemical Physics* **15**, 15062-15077 (2013).

49 van Duin, A. C., Baas, J. M. & Van De Graaf, B. Delft molecular mechanics: a new approach to hydrocarbon force fields. Inclusion of a geometry-dependent charge calculation. *Journal of the Chemical Society, Faraday Transactions* **90**, 2881-2895 (1994).

50 Verstraelen, T., Ayers, P., Van Speybroeck, V. & Waroquier, M. ACKS2: Atom-condensed Kohn-Sham DFT approximated to second order. *The Journal of chemical physics* **138** (2013).

51 Mortier, W. J., Ghosh, S. K. & Shankar, S. Electronegativity-equalization method for the calculation of atomic charges in molecules. *Journal of the American Chemical Society* **108**, 4315-4320 (1986).

52 Kresse, G. & Furthmüller, J. Efficient iterative schemes for ab initio total-energy calculations using a plane-wave basis set. *Physical review B* **54**, 11169 (1996).

53 Blöchl, P. E. Projector augmented-wave method. *Physical review B* **50**, 17953 (1994).